



Article

Antarctic Firn Characterization via Wideband Microwave Radiometry

Rahul Kar 1,* , Mustafa Aksoy 1, Dua Kaurejo 1, Pranjal Atrey 2 and Jerusha Ashlin Devadason 3

- Department of Electrical and Computer Engineering, University at Albany—State University of New York, Albany, NY 12222, USA; maksoy@albany.edu (M.A.); dkaurejo@albany.edu (D.K.)
- Department of Electrical & Computer Engineering, University of Maryland, College Park, College Park, MD 20742, USA; patrey@terpmail.umd.edu
- The State of Utah, Salt Lake City, UT 84111, USA; jdevadason@albany.edu
- * Correspondence: rkar@albany.edu; Tel.: +1-518-466-6504

Abstract: Recent studies have demonstrated that wideband microwave radiometers provide significant potential for profiling important subsurface polar firn characteristics necessary to understand the dynamics of the cryosphere and predict future changes in ice and snow coverage. Different frequencies within the wide spectra of radiometers result in different electromagnetic propagation losses and thus reveal characteristics at different depths in ice and snow. This paper, expanding on those investigations, explores the utilization of the Global Precipitation Measurement (GPM) constellation as a single wideband (6.93 GHz–91.655 GHz) spaceborne radiometer, covering the entire microwave spectrum from C-band to W-band, to profile subsurface properties of the Antarctic firn. Results of the initial analyses over Concordia and Vostok Stations in Antarctica indicate that GPM brightness temperature measurements provide critical information regarding the subsurface temperatures and physical properties of the firn from the surface down to several meters of depth. Considering the high spatiotemporal coverage of polar-orbiting spaceborne radiometers, these results are promising for future continent-level thermal and physical characterization of the Antarctic firn.

Keywords: cryosphere; global precipitation measurement; GPM; microwave radiometry; remote sensing; polar firn



Citation: Kar, R.; Aksoy, M.; Kaurejo, D.; Atrey, P.; Devadason, J.A.
Antarctic Firn Characterization via
Wideband Microwave Radiometry.
Remote Sens. 2022, 14, 2258. https://doi.org/10.3390/rs14092258

Academic Editors: Anshuman Bhardwaj, Lydia Sam and Saeideh Gharehchahi

Received: 20 March 2022 Accepted: 5 May 2022 Published: 7 May 2022

Publisher's Note: MDPI stays neutral with regard to jurisdictional claims in published maps and institutional affiliations.



Copyright: © 2022 by the authors. Licensee MDPI, Basel, Switzerland. This article is an open access article distributed under the terms and conditions of the Creative Commons Attribution (CC BY) license (https://creativecommons.org/licenses/by/4.0/).

1. Introduction

Understanding the behavior of polar ice sheets and glaciers and predicting future changes in their volume and masses are critical to characterize weather, climate, and the water cycle on Earth [1,2]. Thus, measurements are collected in these distant parts of our planet with the help of ground-based meteorological and research stations as well as remote sensing instruments. Due to the extreme environmental conditions associated with polar regions, airborne and spaceborne remote sensing are the most suitable techniques for observing geophysical quantities of the cryosphere and monitoring their temporal and spatial variations [3]. Among remote sensing instruments, satellite-based microwave radiometers have many advantages. Firstly, their measurements are highly sensitive to snow and ice properties such as temperature, density, and grain size; and secondly, they provide data mostly independent of cloud conditions and solar illumination at least twice a day over the entire Antarctic and Arctic regions, whereas in situ measurements are sparse, challenging, and costly [4,5].

Recent studies in passive microwave remote sensing have suggested that the subsurface properties of polar ice layers can be profiled as a function of depth using wideband radiometers by combining electromagnetic forward emission models with plausible models of depth-dependent physical properties [6–8]. This is possible because electromagnetic penetration depth changes with frequency in ice, and different frequency channels of wideband radiometers are sensitive to different depths. One example is the Ultrawideband

Remote Sens. 2022, 14, 2258 2 of 23

Software-Defined Microwave Radiometer (UWBRAD), a 0.5 GHz to 2 GHz microwave radiometer developed at Ohio State University. UWBRAD was deployed on an aircraft, collected brightness temperature measurements over the Greenland Ice Sheet, and led to accurate retrieval of internal temperature profiles from the shallow ice to the bedrock using a Bayesian estimation framework with standard deviations less than 1 K even in the presence of radio frequency interference [9,10]. Following in the footsteps of these efforts and to inspire future radiometer designs to study the polar regions, this article discusses the potential of microwave radiometry to characterize the Antarctic firn, the most vulnerable portion of Earth's largest ice sheet, by utilizing spaceborne radiometer measurements available at higher frequencies across a wider spectrum. The Global Precipitation Measurement (GPM) satellite constellation is employed as a single wideband, multifrequency (11 frequency channels at 6.93 GHz, 7.3 GHz, 10.65 GHz, 18.7 GHz, 19.35 GHz, 22.235 GHz, 23.8 GHz, 36.5 GHz, 37 GHz, 89 GHz, and 91.665 GHz) microwave radiometer system to probe the firn in terms of its thermal and physical properties, such as internal temperature, density, and grain size. These properties are important indicators for the polar ice mass balance and climate [11–15], therefore their retrieval versus depth through spaceborne microwave radiometry with high spatiotemporal coverage may significantly advance polar studies. Estimation of geophysical parameters related to the firn density and grain size using passive microwave remote sensing have been discussed previously, where brightness temperatures at frequencies between 11 GHz and 37 GHz, i.e., from X-band to Ka-band, were utilized [3,16–18]. Although brightness temperature simulations, with some empirical adjustments, matched satellite measurements and retrievals were consistent with in situ measurements in these studies, limited number of frequency channels as well as the overall bandwidth hindered the vertical resolution and range of the retrievals. For instance, although density and grain size variations with depth have been determined to be the main factor in brightness temperature changes, these variations are defined by single depth-independent factors validated within the top few meters of the firn. This article, on the other hand, presents the first attempt in which the entire microwave spectrum from C-band to W-band, with brightness temperature measurements at several frequencies within this wide band, is utilized to be able to characterize such properties from the surface to the deep firn, i.e., tens of meters down from the surface, with a finer vertical resolution allowing changes in density and grain size variations versus depth.

The paper is structured as follows. Section 2 provides information about the models, methods, and data sources used in this study by briefly summarizing the physical, thermal, and electrical properties of the polar firn, the radiation model developed to simulate the firn brightness temperatures to compare with satellite measurements, and the microwave radiometers in the GPM constellation which could be employed for polar firn observations. Section 3 presents the results of analyses focusing on Concordia and Vostok Stations in Antarctica, including satellite measurements, radiation simulations, and retrieval studies. Finally, Section 4 discusses the main conclusions of the study as well as future research plans.

2. Materials and Methods

2.1. Physical, Thermal, and Electrical Properties of the Polar Firn

The polar firn can be considered as a planar layered medium, as illustrated in Figure 1, where each layer is described by its temperature, density, and grain size [19]. Sections 2.1.1–2.1.5 describe the depth-dependent models for these layer parameters used in this study.

2.1.1. Firn Density

The average firn density $\overline{\rho}(z)$ increases exponentially with depth and can be expressed as:

$$\overline{\rho}(z) = \rho_{\infty} - (\rho_{\infty} - \rho_0)e^{z\beta} \text{ kg/m}^3$$
 (1)

where $\rho_0 = \rho(z=0)$ is the near surface density, ρ_∞ is the compacted ice density in deep ice, z (a negative value) is depth, and β is a factor that controls the saturation rate of the

Remote Sens. 2022, 14, 2258 3 of 23

density profiles. Finer scale density fluctuations due to internal layering, $\tilde{\rho}(z)$, on the other hand, can be described as correlated damped noise:

$$\widetilde{\rho}(z) = \rho_n(z)e^{z\alpha} \text{ kg/m}^3,$$
 (2)

where α is the damping factor and $\rho_n(z)$ is the correlated noise which can be modeled as a Gaussian random process with a standard deviation, $\sigma_{density}(z)$, and vertical correlation length, l, as follows:

$$\langle \rho_n(z), \rho_n(z') \rangle = \left(\sigma_{density}(z)\right)^2 \left(-(z-z')^2/l^2\right)$$
 (3)

where $\sigma_{density}(z)$ may vary with depth in a random manner based on time-dependent snow accumulation and compaction processes. As a result, the vertical density profile of the polar firn, $\rho(z)$, can be expressed as the sum of the average firn density and the fluctuations due to layering [20]:

$$\rho(z) = \overline{\rho}(z) + \widetilde{\rho}(z) = \rho_{\infty} - (\rho_{\infty} - \rho_{0})e^{z\beta} + \rho_{n}(z)e^{z\alpha} \text{ kg/m}^{3}$$
(4)

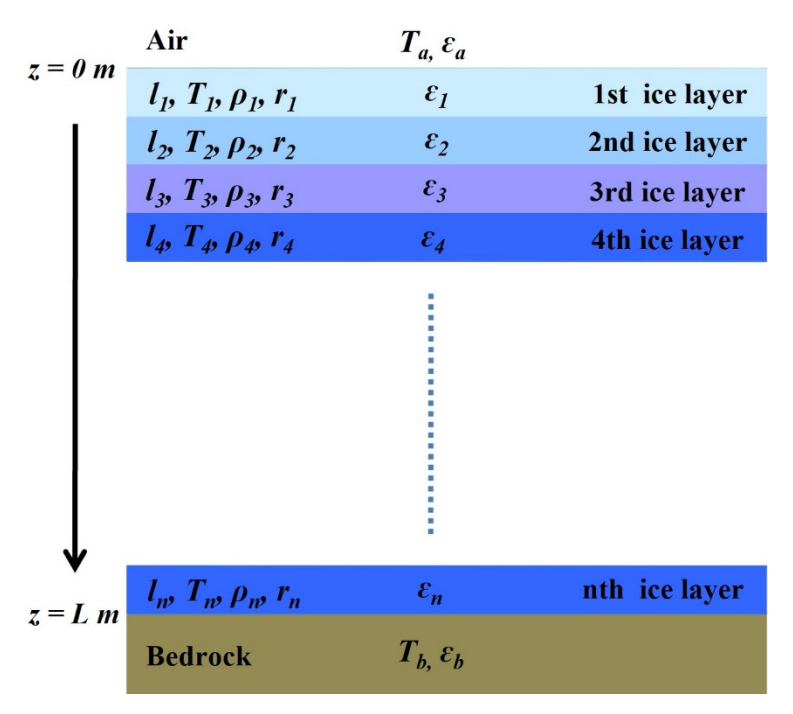


Figure 1. Vertical structure of layered polar firn. Each layer is defined by its length (l), temperature (T), density (ρ), and snow grain radius (r). These parameters lead to unique complex permittivity (ε) values for each layer.

2.1.2. Grain Size

Analyses of in situ grain size measurements in the Antarctic firn have revealed that the depth-dependent ice grain radius can be described by the following model:

$$r(z) = \sqrt{r_o^2 + z \times g_r} \text{ mm}$$
 (5)

where r(z) is the grain radius profile versus depth, r_0 is the grain radius at the surface in millimeters, z is depth in meters, g_r is the grain size gradient in square millimeters per meter. In situ measurements have also demonstrated that the size of ice particles at Concordia is almost double that of at Vostok, as shown in Figure 2 [21,22]. In this study,

Remote Sens. 2022, 14, 2258 4 of 23

using linear regression fits to these measurements, grain radius profiles at Concordia and Vostok Stations, locations of which can be seen in Figure 3, have been modeled as:

$$r_{concordia}(z) = \sqrt{(0.5687)^2 + z \times (5.074 \times 10^{-3})} \text{ mm}$$
 (6)

$$r_{vostok}(z) = \sqrt{(10^{-3})^2 + z \times (9.245 \times 10^{-4})} \text{ mm}$$
 (7)

respectively. However, it is important to note that the fit for Vostok Station is susceptible to errors due to a lack of sufficient depth resolution in in situ measurements, notably for shallower firn. Finally, these grain size profiles are multiplied by an empirical factor $\phi(z)$, a function of depth, to achieve a good match between simulations and spaceborne radiometer measurements, an adjustment similar to the one described in [3].

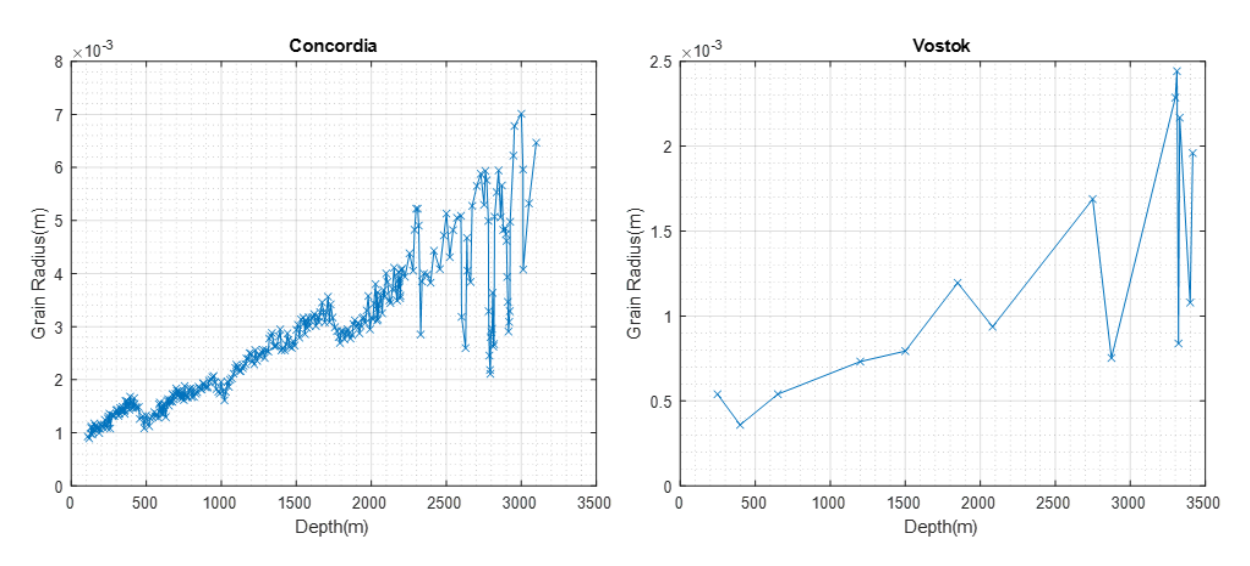


Figure 2. In situ measurements of ice grain size versus depth at (**left**) Concordia and (**right**) Vostok Stations. Data have been obtained from [21,22].

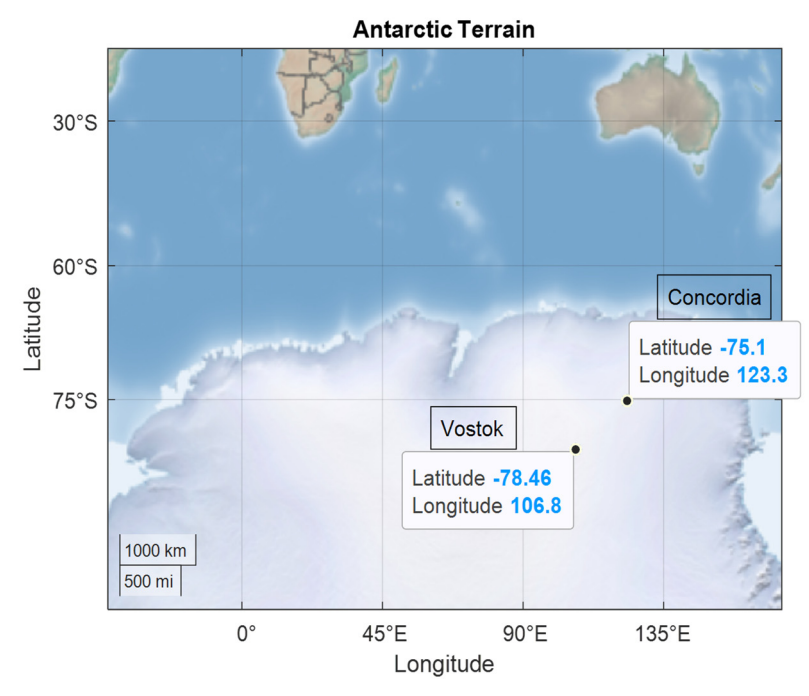


Figure 3. Locations of Concordia and Vostok Stations in Antarctica.

Remote Sens. 2022, 14, 2258 5 of 23

2.1.3. Firn Temperature

Monthly average physical temperature profiles measured at Concordia Station between 2006 and 2010 down to 21 m depth [16], shown in Figure 4, have been considered as ground truth firn temperature data for this study. As shown in the figure, below 21 m, deep ice has been accepted as isothermal with no seasonal temperature variations.

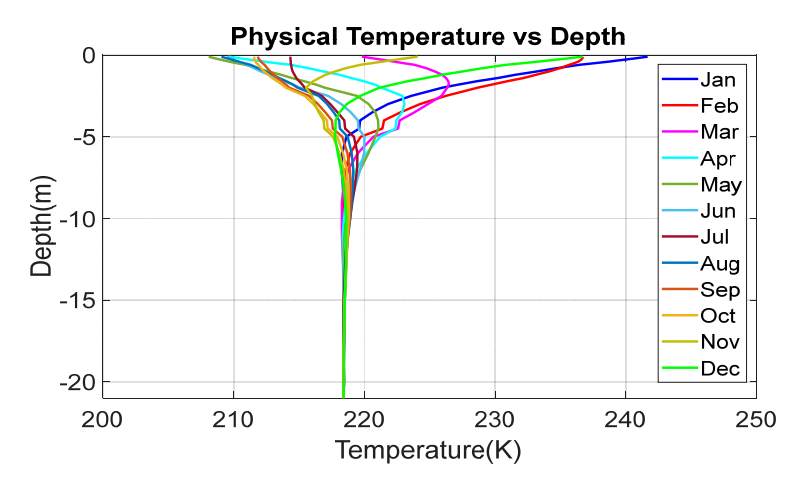


Figure 4. Monthly averaged in situ firn temperature measurements versus depth at Concordia Station between 2006 and 2010. Data have been obtained from [16].

2.1.4. Complex Permittivity

Complex permittivity of pure ice grains, ε_{ice} , has been modeled for microwave frequencies (1–200 GHz) in cold temperatures (<240 K) by Matzler and Wegmuller in [23] and Matzler in [24] as a function of temperature and frequency:

$$\varepsilon_{ice} = 3.1884 + 0.0091(T - 273) + i\left(\frac{\alpha}{f_{GHz}} + \beta f_{GHz}\right),$$
 (8)

where

$$\alpha = \left[0.00504 + 0.0062 \left(\frac{300}{T} - 1\right)\right] e^{\left[-22.1\left(\frac{300}{T} - 1\right)\right]},$$

$$\beta = \frac{0.0207}{T} \frac{e^{\frac{335}{T}}}{\left(e^{\frac{335}{T}} - 1\right)^2} + 1.1610^{-11} f_{GHz}^2 + e^{\left[-9.963 + 0.0372(T - 273.16)\right]},$$

T is the temperature in K, and f_{GHz} is the frequency in GHz.

Figure 5 depicts the electromagnetic penetration depth, i.e., the distance in which the radiation drops to 1/e of its initial value, in pure ice versus temperature and frequency calculated using this complex permittivity model. As shown in the figure, electromagnetic radiation can propagate longer distances in colder ice and at lower frequencies. At 240 K and 1 GHz, for example, the penetration depth is higher than 100 m, whereas it drops to a few tens of centimeters when the frequency increases to 100 GHz. Thus, although the polar firn is not pure ice and internal layering and scattering may affect electromagnetic propagation, it can be accepted that the penetration depth varies significantly with frequency, so wideband or multichannel radiometers can profile firn properties versus depth as different frequencies in their operational spectrum are sensitive to different layers.

2.1.5. Effective Permittivity

Using the physical temperature, density, and grain size information described in the previous subsections, effective complex permittivity of a firn layer at depth z, $E_{eff}(z)$, can

Remote Sens. 2022, 14, 2258 6 of 23

be calculated as described in [25,26] by defining the effective complex permittivity without scattering effects, $E_{eff0}(z)$, as the solution of the following quadratic equation:

$$E_{eff0}(z)^2 + E_{eff0}(z) \left(\frac{\varepsilon_s - \varepsilon_b}{3} \left(1 - 4v_f(z) \right) - \varepsilon_b \right) - \varepsilon_b \frac{\varepsilon_s - 1}{3} \left(1 - v_f(z) \right) = 0$$
 (9)

where $v_f(z)$ is the fractional volume of scatterers (ice grains) at depth z, and ε_b and ε_s are dielectric constants of the background (air) and scatterers (ice as described in Equation (8)), respectively. If the scattering effects are included the complex permittivity, $E_{eff}(z)$, becomes:

$$E_{eff}(z) = \varepsilon_b + \left(E_{eff0}(z) - \varepsilon_b\right) \left[1 + i\frac{2}{9} (k_0 r(z))^3 \sqrt{E_{eff0}(z)} (\varepsilon_s - \varepsilon_b) + \frac{\varepsilon_s - \varepsilon_b}{3E_{eff0}(z)} \frac{\left(1 - v_f(z)\right)^5}{\left(1 + 2v_f(z)\right)^2} \right]$$
(10)

where $k_0 = 2\pi/\lambda$ is the wavenumber, λ is the wavelength, and r(z) is the radius of ice grains.

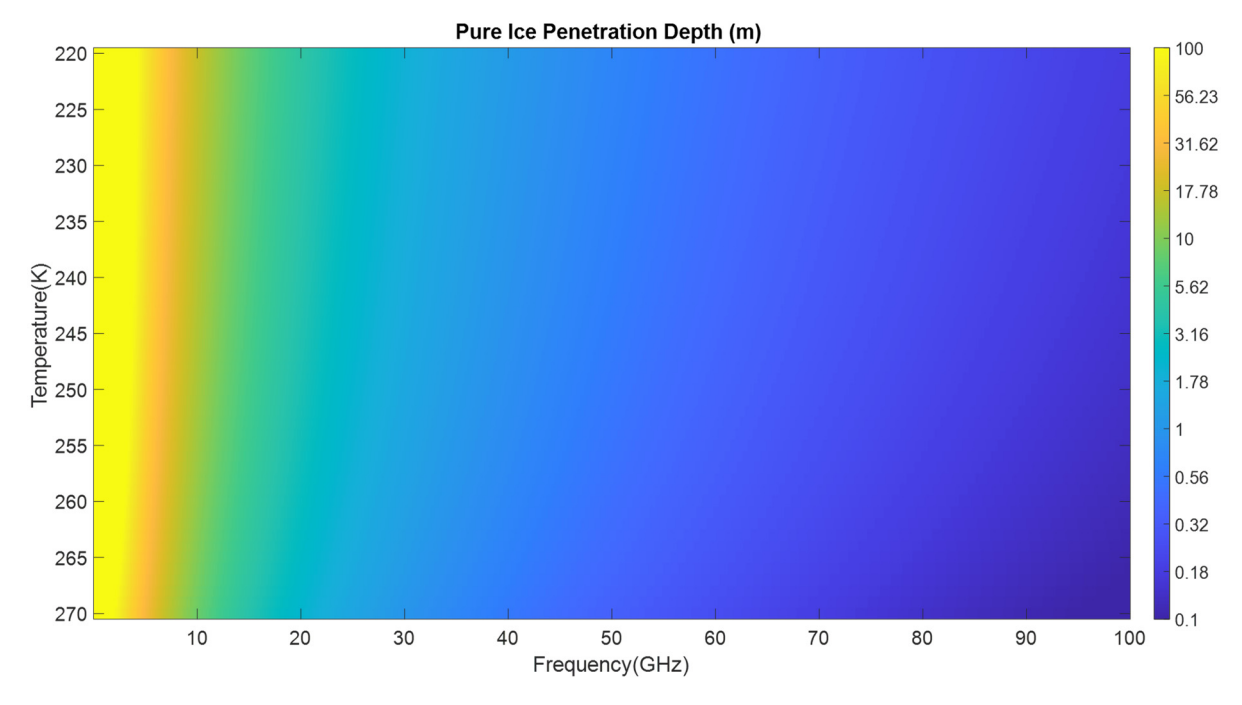


Figure 5. Electromagnetic penetration depth (in meters) in pure ice versus temperature and frequency below 100 GHz. Note the increase in penetration depth with lower frequencies and temperatures.

2.2. Radiation Model

A simple microwave radiation model has been developed, and the brightness temperatures at the firn surface for frequency f, incidence angle θ_i , and polarization p, $T_B(z=0,f,\theta_i,p)$ have been analytically calculated using the following zeroth-order radiative transfer equation:

$$T_{B}(z=0,f,\theta_{i},p) = \int_{z_{deep}}^{z=0} \left[\prod_{z'=z}^{z'=0} \Gamma(z',\theta(z'),p) \right] \kappa_{e}(f,z) \sec \theta(z) T(z) e^{-\int_{z'=z}^{z'=0} \kappa_{e}(z',f) \sec \theta(z') dz'} dz$$
 (11)

where $\Gamma(z',\theta(z'),p)$, $\theta(z')$, and T(z) are the amplitude squared of the Fresnel transmission coefficient at the ice layer interface at depth z' for polarization p, the angle of incidence at the ice layer interface at depth z', and the physical firn temperature at depth z, respectively. κ_e is the extinction coefficient. Notice that Equation (11) follows the expressions given in [25–27] with improvements to consider the effects of incidence angle, polarization, and internal reflections due to density fluctuations among ice layers. This equation can also be written as:

$$T_B(z = 0, f, \theta_i, p) = \int_{z_{does}}^{z=0} W(f, \theta, p, z) T(z) dz$$
 (12)

Remote Sens. 2022, 14, 2258 7 of 23

where

$$W(f,\theta,p,z) = \left[\prod_{z'=z}^{z'=0} \Gamma(z',\theta(z'),p) \right] \kappa_e(f,z) \sec \theta(z) e^{-\int_{z'=z}^{z'=0} \kappa_e(z',f) \sec \theta(z') dz'}$$
(13)

is the weight function for frequency f, incidence angle θ , and polarization p. The extinction coefficient κ_e can be calculated here as the sum of scattering and absorption coefficients, κ_s and κ_a , with the help of an existing microwave emission model called Microwave Emission Model of Layered Snowpacks (MEMLS). MEMLS has been developed by Mätzler and Wiesmann [27] across microwave frequencies from 5 GHz to 100 GHz. It is a radiative transfer model which uses six-flux theory for describing multiple volume scattering and absorption, including radiation trapping due to internal reflection and a combination of coherent and incoherent superposition of reflections between layer interfaces. The absorption coefficient of a layer at depth z can be computed using the effective complex permittivity E_{eff} as:

$$\kappa_a(z) = 4\pi \times \frac{\mathrm{imag}\left(\sqrt{E_{eff}(z)}\right)}{\lambda_o}$$
(14)

where λ_o is the wavelength in a vacuum. To determine the scattering coefficient, an exponential correlation length, p_{ec} , which is related to the snow grain size r(z) should be found. First, r_{max} , the maximum extension of the prevailing grain size r(z) in millimeters, has been determined using the following equation [28] to reduce the variations in large values of the observed firn grain radius:

$$r(z) = 1.5 \times \left(1 - e^{(-1.5 * r_{max})}\right)$$
 (15)

Then, the exponential correlation length in millimeters can be derived from r_{max} as follows:

$$p_{ec} = \begin{cases} a_0 + a_1 ln(r_{max}) \pm \varepsilon_{fit} & \text{if } r_{max} > r_{small} \\ p_0 \pm \varepsilon_0, & \text{otherwise} \end{cases}$$
 (16)

where a_0 and a_1 are two empirical fitting factors, and r_{small} is the threshold for small grain size. ε_{fit} and ε_0 represent the error and the uncertainty associated with the resulting fit, respectively. This method was introduced in [29] by analyzing the microstructure of snow samples from Weissflühjoch, Davos, Switzerland. In this study, the values for a_0 , a_1 , p_0 , r_0 , ε_{fit} , and ε_0 were taken as 0.18 mm, 0.09 mm, 0.05 mm, 0.125 mm, 0.027 mm, and 0.017 mm, respectively. Once p_{ec} is obtained, the scattering coefficient within a layer at depth z can be calculated from snow physical properties [27,30] as follows:

$$\kappa_s(z) = \left(\frac{9.2p_{ec}}{1\text{mm}} - \frac{1.23\rho(z)}{1\text{gm/cm}^3} + 0.54\right)^{2.5} \times \left(\frac{f}{50\text{GHz}}\right)^{2.5}$$
(17)

where $\rho(z)$ is the firn density as described in Equation (4) and f is the radiation frequency in GHz.

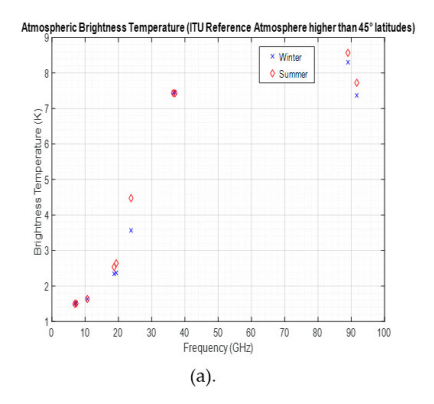
Atmospheric Attenuation

The radiation model defined by Equation (11) outputs the surface brightness temperature of the Antarctic firn, i.e., microwave radiation from the firn surface; however, atmospheric contributions and losses are not taken into account. Thus, the Rec ITU-R P.835-6 [31] expressions and data for reference standard atmospheres have been followed for estimating the atmospheric attenuation and brightness temperatures to calculate the top of the atmosphere brightness temperature, $T_{B_{TOA}}$, as:

$$T_{B_{TOA}}(f) = T_B(z = 0, f, \theta_i, p) \times K(f) + T_{B_{ATM}}(f)$$
 (18)

Remote Sens. 2022, 14, 2258 8 of 23

where K(f) is the atmospheric attenuation factor as a function of frequency and $T_{B_{ATM}}$ is the atmospheric brightness temperature. The reference standard atmospheres have been utilized to determine temperature, pressure, and humidity as a function of altitude for calculating gaseous attenuations when local data are not available. To determine the atmospheric attenuation around Concordia Station (75°05′59″ S 123°19′56″ E) in Antarctica, the high latitude reference atmosphere defined for summer and winter seasons has been used. Figure 6 demonstrates the atmospheric brightness temperatures and attenuation factors used in this study to calculate the top of the atmosphere brightness temperatures over the Antarctic firn versus frequency.



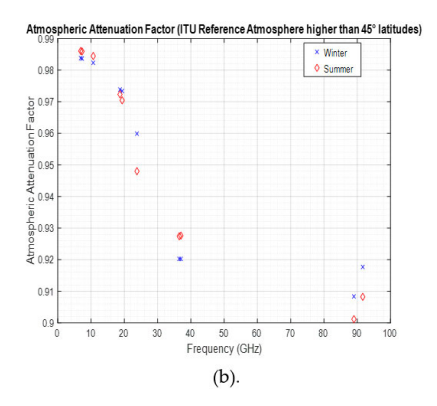


Figure 6. (a) Atmospheric brightness temperature and (b) atmospheric attenuation factor versus frequency based on the high latitude reference atmosphere defined in Rec ITU-R P.835-6.

2.3. Global Precipitation Measurement Mission

The Global Precipitation Measurement (GPM) mission, shown in Figure 7, is an international constellation-based mission designed to combine and improve precipitation measurements from several operational microwave sensors. None of the GPM members were built and launched specifically for the GPM mission. The individual satellites were designed and deployed by their respective space agencies for their own weather programs, but the international community, led by the National Aeronautics and Space Administration (NASA) and the Japan Aerospace Exploration Agency (JAXA), decided to incorporate the measurements from these satellites for consistent precipitation products with larger global coverage [32,33].

Within the GPM constellation, Special Sensor Microwave Imager/Sounder (SSMIS) on Defense Meteorological Satellite Program (DMSP) satellites F16, F17, F18, F19, and F20 (operated by NASA and the National Oceanic and Atmospheric Administration (NOAA)) and Advanced Microwave Scanning Radiometer-2 (AMSR2) on the Global Change Observation Mission-Water 1 (GCOM-W1) satellite (operated by JAXA) provide radiometric measurements over the polar regions at frequencies below 100 GHz where the electromagnetic penetration depth varies between tens of meters and a few centimeters, as shown in Figure 5. Thus, measurements provided by these two sets of instruments are suitable for the study of the polar firn and have been analyzed in this paper. The main characteristics of the SSMIS and AMSR2 radiometers are summarized in Sections 2.3.1 and 2.3.2.

2.3.1. Special Sensor Microwave Imager/Sounder (SSMIS)

The Special Sensor Microwave Imager/Sounder (SSMIS) is a 24-channel microwave radiometer with channel frequencies ranging from 19.35 GHz to 183 GHz [35]. It measures brightness temperatures at a 53.1° incidence angle in horizontal and vertical polarizations with sampling intervals varying from 12.5 km to 37.5 km (note that the 22.235 GHz channel provides measurements only in vertical polarization).

Remote Sens. 2022, 14, 2258 9 of 23

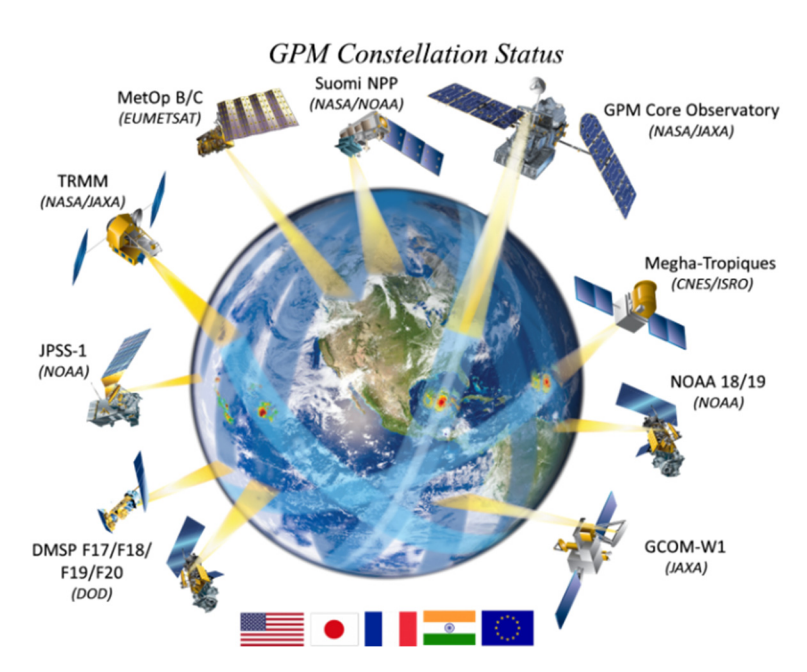


Figure 7. The Global Precipitation Measurement (GPM) constellation and member satellites with corresponding governmental space agencies. The figure is taken from [34].

2.3.2. Advanced Microwave Scanning Radiometer-2 (AMSR2)

The Advanced Microwave Scanning Radiometer-2 (AMSR2) is a seven-frequency radiometer which provides measurements at a fixed 55° incidence angle [36,37]. It measures brightness temperatures in both vertical and horizontal polarizations at 6.9 GHz, 7.3 GHz, 10.65 GHz, 18.7 GHz, 23.8 GHz, 36.5 GHz, and 89 GHz with spatial resolutions ranging from 3 km \times 5 km to 35 km \times 62 km.

2.3.3. Intercalibration of the GPM Constellation

The GPM Intersatellite Calibration Working Group (XCAL team) was established in 2007 within the NASA Precipitation Measurement Missions (PMM) science team and is responsible for providing intercalibrated brightness temperature products for the GPM constellation. This intercalibration process which merges the constellation sensors as a single multifrequency radiometer involves several steps. First, the biases across the antenna scan or along the satellite orbit are removed for each instrument. Then, channels from different instruments at similar frequencies are compared, accounting for differences in center frequencies, bandwidths, polarizations, and view angles using radiative transfer models. For frequency channels where the atmosphere is semi-transparent, two-point calibration adjustment is performed using overlapping measurements over oceans (cold target) and high-emissivity vegetated lands (warm target). For frequencies insensitive to the surface, only one-point adjustment is performed [38]. GPM Microwave Imager (GMI), another instrument in the GPM constellation, is taken as a calibration reference for these adjustments.

GPM intercalibrated brightness temperatures are produced by the XCAL team and made publicly available on NASA Goddard Space Flight Center's Precipitation Processing System (PPS) website [39]. The datasets include SSMIS's 19.35 GHz, 22.235 GHz, 37 GHz, and 91.655 GHz channels as well as AMSR2's 10.65 GHz, 18.7 GHz, 23.8 GHz, 36.5 GHz, and 89 GHz channels (see Figure 8). Thus, measurements performed by these channels can be considered as multi-frequency observations by a single wideband spaceborne radiometer.

Instrument	AMSR2	AMSR2	SSMIS	SSMIS	AMSR2	AMSR2	SSMIS	AMSR2	SSMIS
Frequency (GHz)	10.65	18.7	19.35	22.235	23.8	36.5	37	89	91.655

Figure 8. GPM-Intercalibrated SSMIS and AMSR2 Channels.

Remote Sens. 2022, 14, 2258 10 of 23

3. Results

3.1. Analyses over Concordia and Vostok Stations in Antarctica

To demonstrate the potential of the GPM constellation as a wideband multi-frequency spaceborne radiometer to characterize the Antarctic firn, an initial analysis has been conducted, and the sensitivity of the SSMIS and AMSR2 intercalibrated multi-frequency radiometer measurements to the thermal and physical properties of the polar firn layers has been investigated at Concordia and Vostok Stations in Antarctica locations of which are shown in Figure 3.

3.1.1. Satellite Measurements

Intercalibrated brightness temperature measurements of AMSR2 and SSMIS radiometers as well as the 6.9 GHz and 7.3 GHz brightness temperature measurements of AMSR2 from January 2020 to June 2021 were collected and averaged monthly over two $0.25^{\circ} \times 0.25^{\circ}$ latitude-longitude grids centered around Concordia ($75^{\circ}05'59''S$ $123^{\circ}19'56''E$) and Vostok ($78^{\circ}27'50''S$ $106^{\circ}50'15''E$) Stations in Antarctica. Intercalibrated brightness temperatures were obtained from the PPS website and the lowest two frequency channel measurements of AMSR2 were downloaded from the Globe Portal System (G-Portal) of JAXA [40]. Monthly averages and large grid cells were considered to reduce the impacts of different sensor overpass times and spatial resolutions as well as intercalibration errors.

Figure 9 depicts the horizontally polarized brightness temperatures versus month, with ranges of ± 1 monthly standard deviations, over Concordia and Vostok Stations between January 2020 and June 2021 at all above-mentioned AMSR2 and SSMIS frequencies (except 22.235 GHz since only vertically polarized brightness temperatures are available at this frequency). Figure 10 demonstrates the same brightness temperatures in vertical polarization. It can be seen from the figures that at low frequencies, e.g., 6.9 GHz, 7.3 GHz, and 10.65 GHz, the brightness temperatures do not vary significantly throughout the year. At higher frequencies, e.g., 89 GHz and 91.65 GHz, on the other hand, the seasonal variations can be as large as 35 K. As expected in the Southern Hemisphere, the maximum brightness temperatures are observed in December–January and the lowest brightness temperatures are measured between May and September. Moreover, due to the lower reflection between ice and air in vertical polarization, vertically polarized brightness temperatures are slightly higher than horizontally polarized brightness temperatures. Finally, except at the two highest frequencies, measurements over Concordia Station have been found to be warmer than those over Vostok Station in both polarizations.

3.1.2. Radiation Simulations

In order to accurately interpret the measured AMSR2 and SSMIS brightness temperatures shown in Figures 9 and 10, a simple simulation was conducted. Monthly averaged physical temperature profiles measured at Concordia Station between 2006 and 2010 down to 21 m depth [16] (shown in Figure 4), and firn density and grain size profiles (described in Section 2.1) were considered in the simulation. Although they may not accurately reflect the properties of the firn layers at Concordia and Vostok Stations in 2020 and 2021, these profiles are consistent with the models described in Equations (4), (6), and (7) in Section 2.1. For the density model in Equation (4), it was assumed that $\rho_{\infty}=922~{\rm kg/m^3}$, $\rho_0=336~{\rm kg/m^3}$, $\beta=0.017~{\rm m^{-1}}$, ρ_n is a Gaussian random process with zero mean and standard deviation which varies randomly with depth, and $\alpha=0.02~{\rm m^{-1}}$. Top of the atmosphere brightness temperatures for Concordia and Vostok Stations were calculated using these parameters using Equations (11) and (18), and to validate these simulations, calculated brightness temperatures at AMSR2 and SSMIS frequencies and incidence angles were compared with AMSR2 and SSMIS brightness temperature measurements.

Remote Sens. 2022, 14, 2258 11 of 23

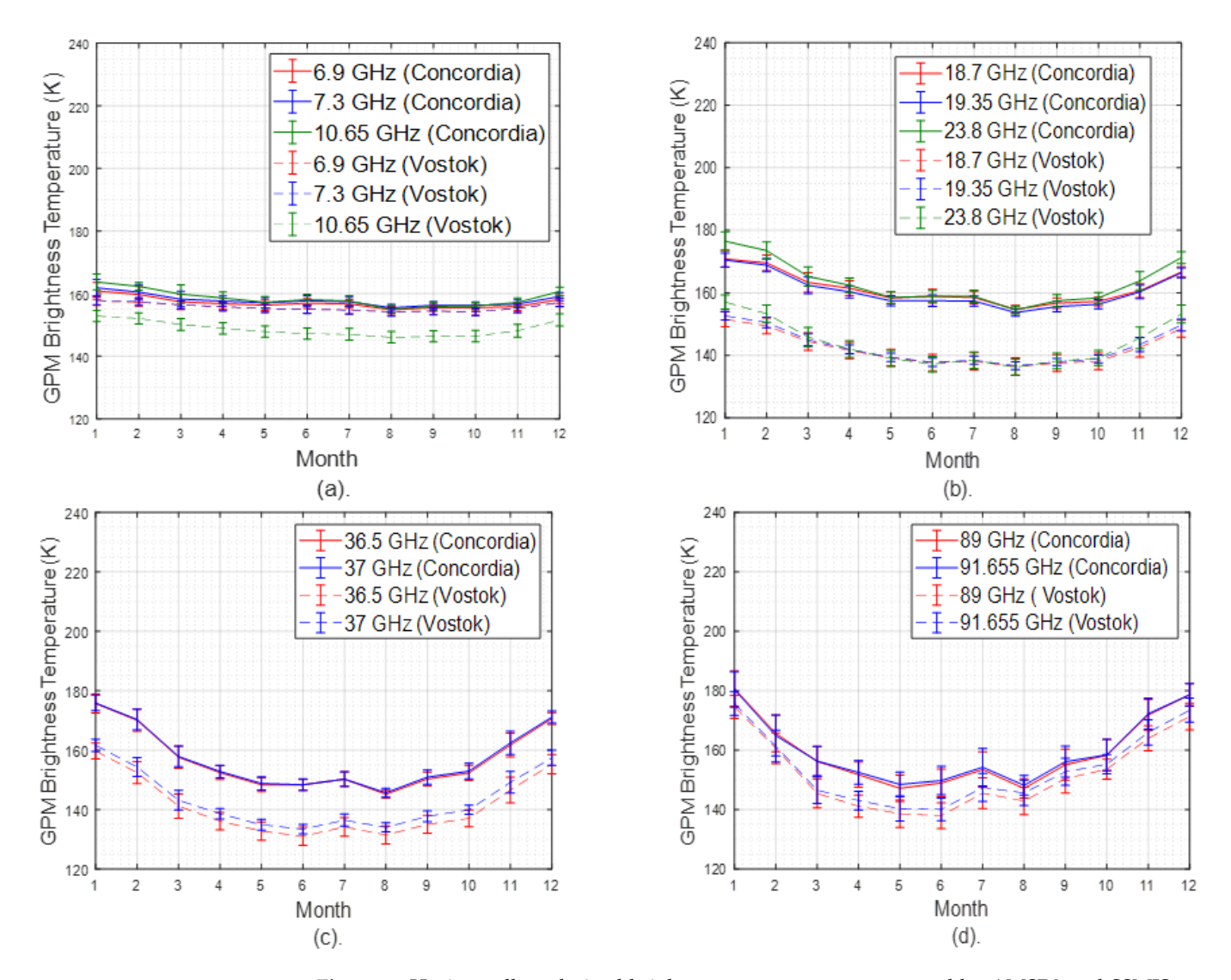


Figure 9. Horizontally polarized brightness temperatures measured by AMSR2 and SSMIS over (solid) Concordia and (dashed) Vostok Stations in Antarctica versus month between 2020 and 2021 at frequencies (a) 6.9 GHz, 7.3 GHz, and 10.65 GHz; (b) 18.7 GHz, 19.35 GHz, and 23.8 GHz; (c) 36.5 GHz and 37 GHz; and (d) 89 GHz and 91.65 GHz. The vertical lines demonstrate the ranges of ± 1 monthly standard deviations. Note that all measurements except those from the 6.9 GHz and 7.3 GHz channels of AMSR2 are intercalibrated and the brightness temperatures were averaged over month and $0.25^{\circ} \times 0.25^{\circ}$ grids.

Figure 11 depicts the calculated top of the atmosphere horizontally polarized brightness temperatures versus month and compares them with AMSR2 and SSMIS measurements shown in Figures 9 and 10. As the in situ firn temperature measurements used for the simulations (see Figure 4) were measured at Concordia Station, AMSR2 and SSMIS observations are shown only for Concordia Station. Additionally, vertical polarization simulations are not discussed here, but they demonstrate similar characteristics. It can be seen in Figure 11 that overall brightness temperature trends are, in general, similar in calculated and measured brightness temperatures. More specifically:

 At 6.9 GHz and 7.3 GHz, both simulated and measured brightness temperatures are almost constant during the year as expected since they are mostly sensitive to layers in isothermal deep firn, as the electromagnetic penetration depth is mostly larger than 20 m and the temperature of layers below this depth does not experience any significant seasonal variations, as shown in Figures 3 and 4. Furthermore, the bias Remote Sens. 2022, 14, 2258 12 of 23

- between the simulations and the measurements is negligible, as their distribution mostly overlaps throughout the year.
- Measured brightness temperatures exhibit 10–20 K seasonal variations at frequencies between 10.65 GHz and 23.8 GHz where the annual mean brightness temperature and the seasonal variations increase with frequency. Simulated brightness, on the other hand, underestimates these seasonal variations. Additionally, at these frequencies, biases up to 10 K have been observed in the annual mean brightness temperatures between simulations and measurements. These two sources of error have led to biases as large as 20 K, specifically at 18.7 GHz.
- Simulations and measurements at 36.5 GHz and 37 GHz agree well except in Antarctic summer (from September to March), where again, the simulations fail to follow the sharp increase in measured brightness temperatures, resulting biases up to ~10 K.
- Finally, measurements and simulations at the highest two frequencies, i.e., 89 GHz and 91.65 GHz, which exhibit the largest seasonal variations (~35 K) mostly agree with each other.

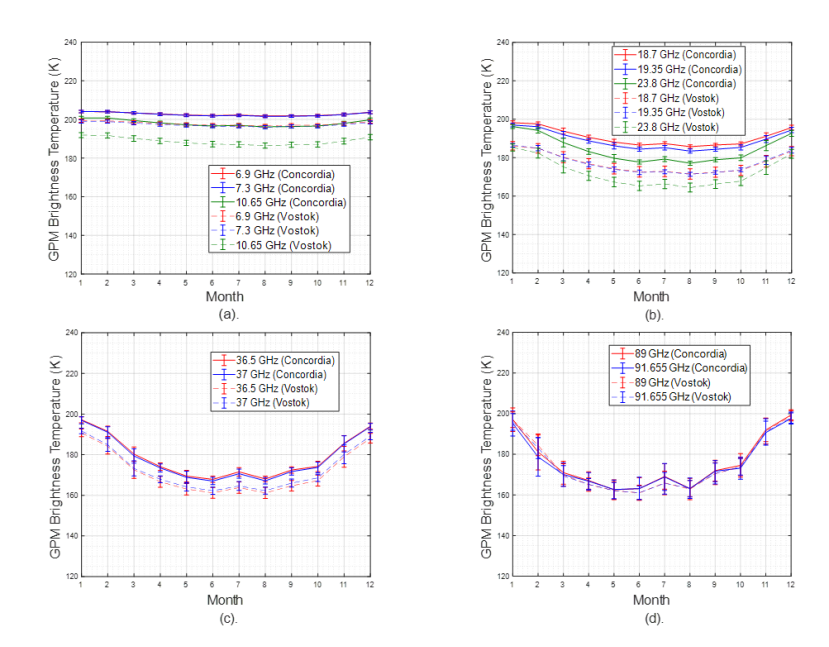


Figure 10. Vertically polarized brightness temperatures measured by AMSR2 and SSMIS over (solid) Concordia and (dashed) Vostok Stations in Antarctica versus month between 2020 and 2021 at frequencies (**a**) 6.9 GHz, 7.3 GHz, and 10.65 GHz; (**b**) 18.7 GHz, 19.35 GHz, and 23.8 GHz; (**c**) 36.5 GHz and 37 GHz; and (**d**) 89 GHz and 91.65 GHz. The vertical lines demonstrate the ranges of ± 1 monthly standard deviations. Note that all measurements except those from the 6.9 GHz and 7.3 GHz channels of AMSR2 are intercalibrated and the brightness temperatures were averaged over month and $0.25^{\circ} \times 0.25^{\circ}$ grids.

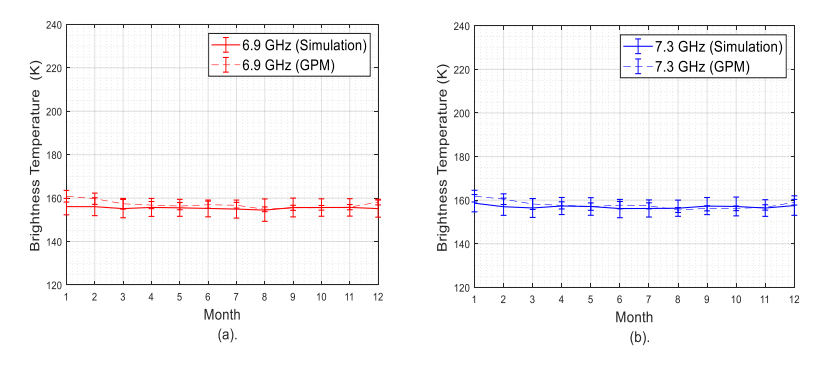


Figure 11. Cont.

Remote Sens. 2022, 14, 2258 13 of 23

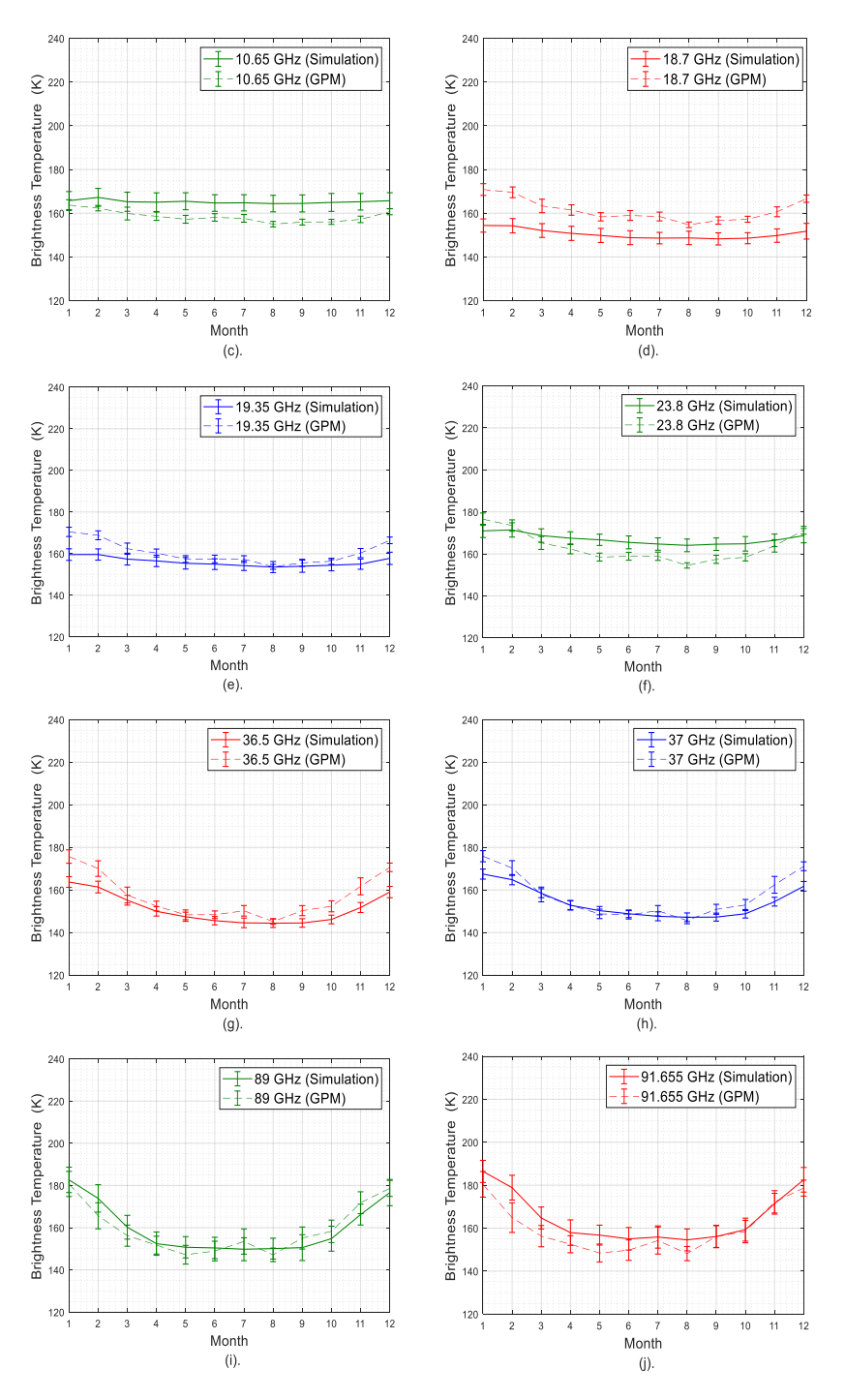


Figure 11. Horizontally measured polarized brightness temperatures over Concordia Station versus simulations as described in Section 3.1.2 at frequencies (a) 6.9 GHz; (b) 7.3 GHz; (c) 10.65 GHz; (d) 18.7 GHz; (e) 19.35 GHz; (f) 23.8 GHz; (g) 36.5 GHz; (h) 37 GHz; (i) 89 GHz, and (j) 91.65 GHz. Note that simulations demonstrate similar seasonal trends with satellite measurements.

3.1.3. Retrieval Studies

To match the simulated top of the atmosphere brightness temperatures over Concordia Station as shown in Figure 11, $\sigma_{density}(z)$ and $\dot{\Phi}(z)$, density and grain size parameters defined in Sections 2.1.1 and 2.1.2 were randomly varied in each layer with high resolution. This can be considered as an initial step for retrieval studies for some of the important physical properties of the Antarctic firn, namely density and grain size profiles. Figure 12 depicts the variation of $\sigma_{density}(z)$ and $\dot{\Phi}(z)$ with depth and the resulting firn density and grain radius

Remote Sens. 2022, 14, 2258 14 of 23

profiles as described in Equations (4) and (6), which have provided a good match between the simulations and satellite measurements, as shown in Figure 11. The optimum $\sigma_{density}(z)$ and $\dot{\Phi}(z)$ profiles were selected by minimizing the root mean square errors between the simulated and measured top of the atmosphere brightness temperatures across all the frequency channels.

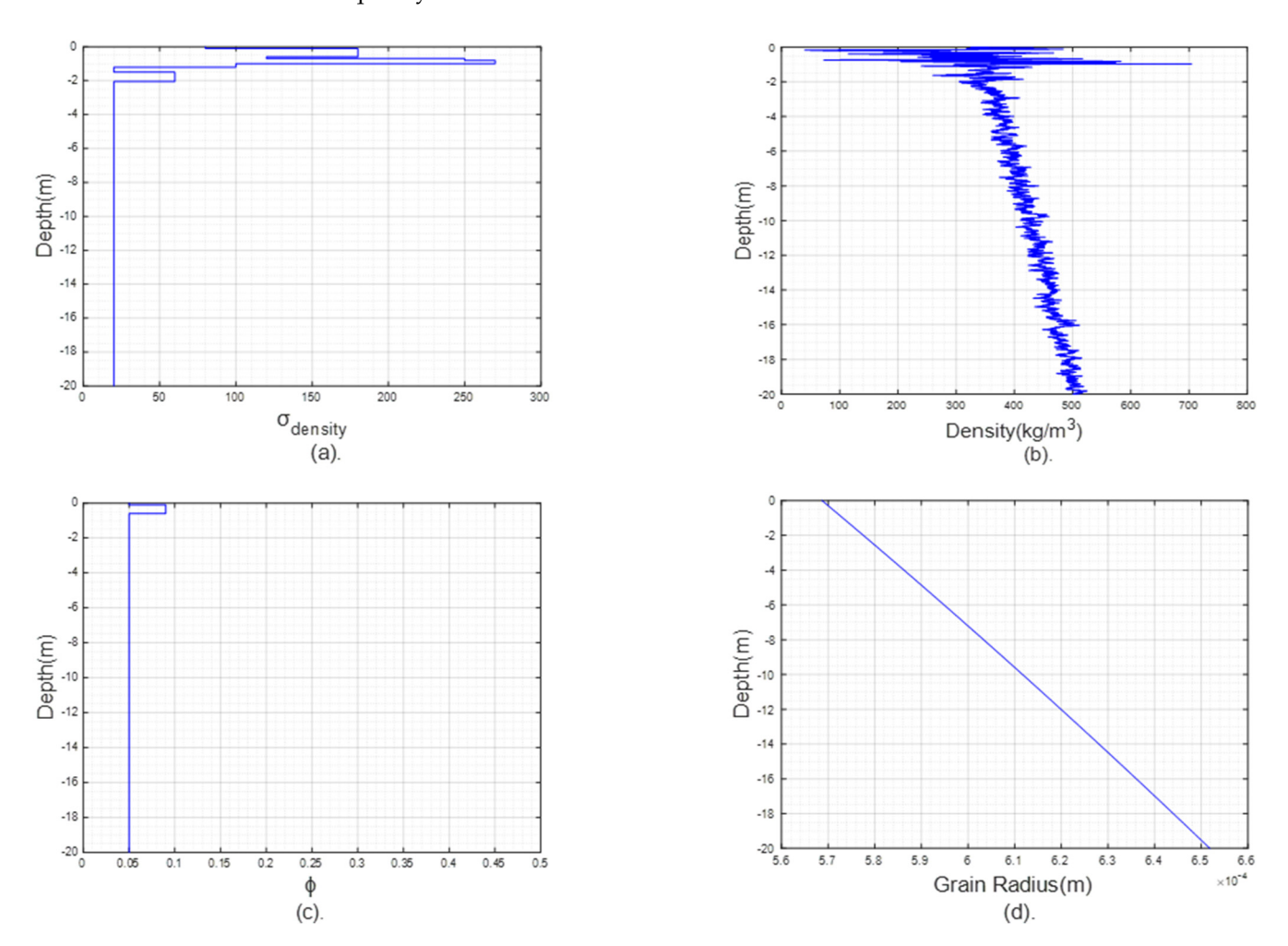


Figure 12. (a) Standard deviation of the firn density fluctuations, $\sigma_{density}(z)$; (b) the resulting firn density, $\rho(z)$, versus depth; (c) the grain radius empirical factor, $\Phi(z)$; and (d) the resulting grain radius profile, $r_{concordia}(z)$, versus depth to match radiation simulations with spaceborne radiometer measurements over Concordia Station as shown in Figure 11.

As seen in Figure 12, the retrieved density fluctuations are larger near the surface and substantially decrease with depth. These thinner near-surface layers with high density fluctuations vs. thicker layers with smoother density profiles, in general, agree with previous in situ density profile measurements performed near Concordia Station [16] except for the fact that larger fluctuations, ~200 kg/m³ peak-to-peak, were obtained in this study compared to ~100 kg/m³ peak-to-peak fluctuations presented in [16]. The retrieved grain radius profile also suggests larger grain radii, ~600 μ m, than the in situ data extrapolated to near surface as described in Section 2.1.2. However, these values are consistent with previous near-surface grain size estimations at and around Concordia Station [17], conforming with our results.

Remote Sens. 2022, 14, 2258 15 of 23

Relative contributions of the firn layers at different depths to the surface brightness temperatures in radiation simulations can be calculated through normalized weight functions, $W_n(f, \theta, p, z)$, as follows:

$$W_n(f,\theta,p,z) = W(f,\theta,p,z) / \int_{z_{deen}}^{z=0} W(f,\theta,p,z) dz$$
 (19)

where $W(f, \theta, p, z)$ is the weight function defined in Equation (13) in Section 2.2. Figure 13 demonstrates the normalized weight functions in horizontal polarization for AMSR2 and SSMIS frequencies and incidence angles calculated assuming Antarctic winter conditions (the June firn temperature profile in Figure 4 was used). Functions in summer conditions and vertical polarization, in general, exhibit similar trends.

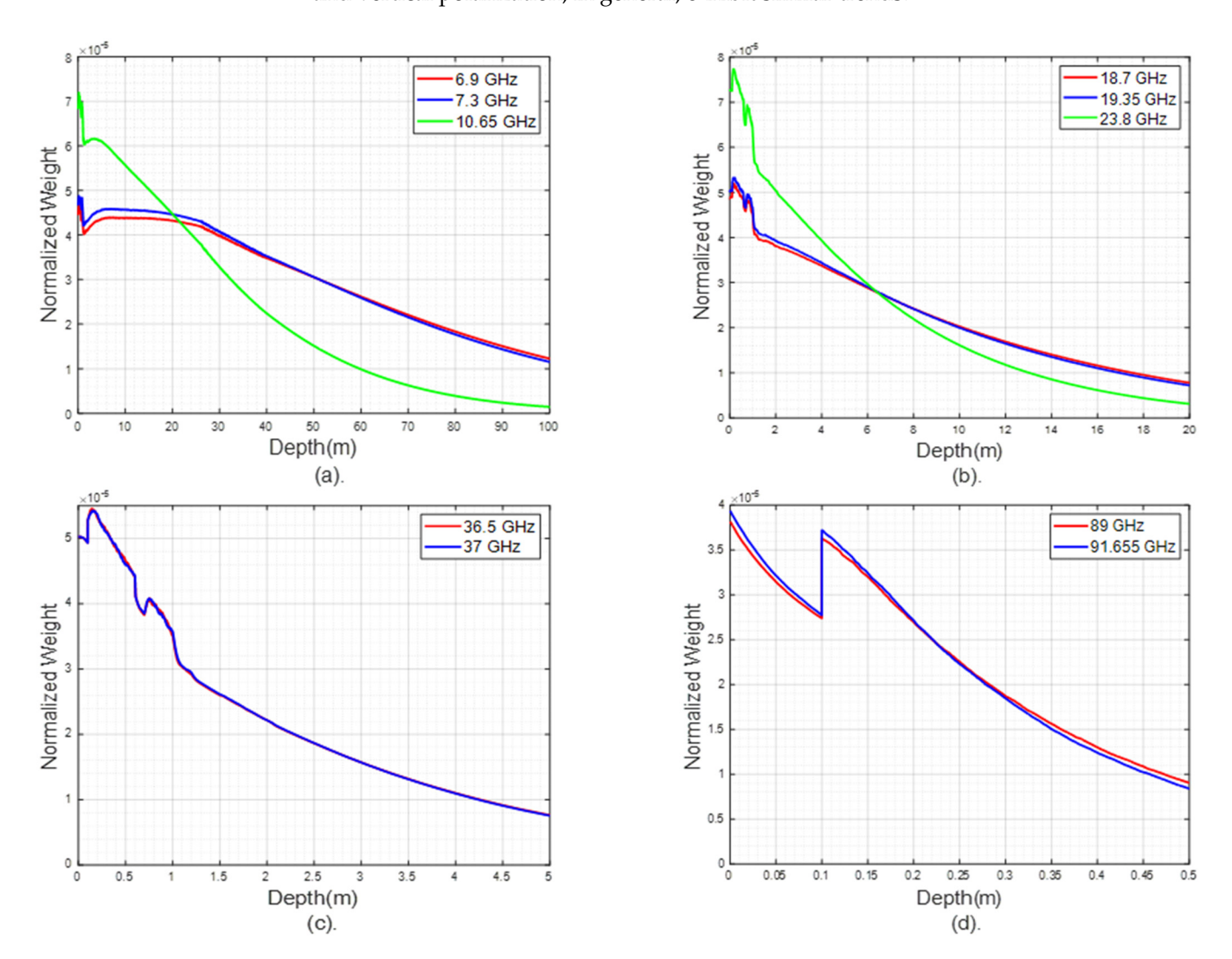


Figure 13. Normalized weight functions versus depth at frequencies (a) 6.9 GHz, 7.3 GHz, and 10.65 GHz; (b) 18.7 GHz, 19.35 GHz, and 23.8 GHz; (c) 36.5 GHz and 37 GHz; and (d) 89 GHz and 91.65 GHz. Note that these functions were calculated using the density and grain size profiles shown in Figure 12.

Figure 13 shows that as the frequency increases, contributions to the surface brightness temperatures become restricted to the layers close to the surface, whereas at low frequencies the contributions are significant even from deep layers. For instance, at 89 GHz and 91.65 GHz, surface layers contribute almost 10 times more to the surface brightness temperature than the layers at 50 cm depth. On the other hand, at 6.9 GHz, layers as deep

Remote Sens. 2022, 14, 2258 16 of 23

as 100 m can substantially influence the surface brightness temperature. To quantitatively describe the depths that characterize surface microwave emissions, a new parameter called average firn depth of sensitivity— $z_{avg}(f, \theta, p)$, a function of frequency, incidence angle, and polarization—has been introduced in this study as follows:

$$0.5 = \int_{z_{deep}}^{z=z_{avg}(f,\theta,p)} W_n(f,\theta,p,z) dz$$
 (20)

Equation (20) indicates that the depth at which firn layers above and below the average depth of sensitivity for a particular frequency are each responsible for half of the surface emissions at that frequency. The average depths of sensitivity in horizontal polarization at AMSR2 and SSMIS frequencies and incidence angles have been calculated and shown in Figure 14. The figure depicts that the average depths of sensitivities decrease from ~41 m to near surface as frequency increases from 6.9 GHz to 91.65 GHz, confirming the potential of wideband or multifrequency radiometry to probe different depths inside the firn. Note that, although decreasing with frequency, these values are significantly smaller than the electromagnetic penetration depths shown in Figure 5. It is expected that the physical properties of the firn at the average depths of sensitivity, rather than electromagnetic penetration depths, exhibit higher correlation with the microwave radiations at the associated frequencies.

Frequency (GHz)	6.9	7.3	10.65	18.7	19.35	23.8	36.5 - 37	89 – 91.65
z_{avg} (m)	~41.4	~37.0	~15.1	~2.1	~2.0	~1.0	~0.2	~0

(a)

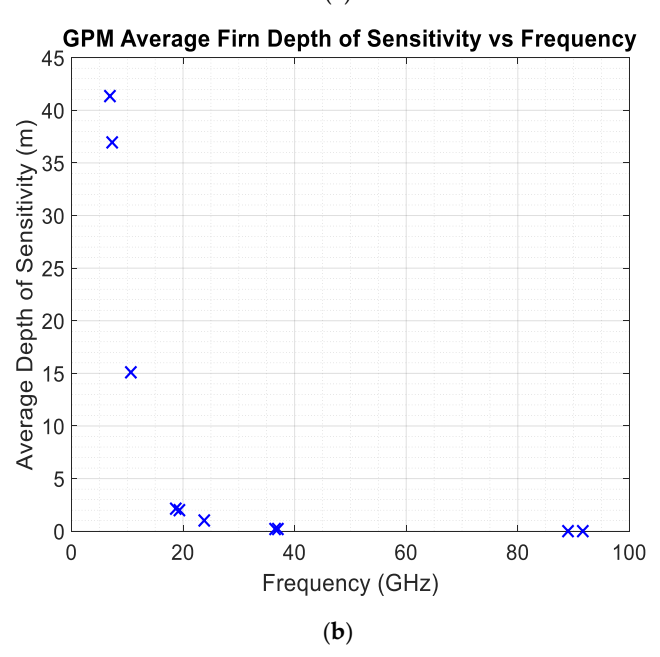


Figure 14. Average firm depths of sensitivity at AMSR2 and SSMIS frequencies and incidence angles as calculated via Equation (20) using the normalized weight functions shown in Figure 13. (a) Table illustrating depth sensitivity values; (b) plot of average depths of sensitivity versus frequency.

3.2. Outcomes

In Section 2.2, a simple microwave emission model has been introduced and validated by comparing simulated brightness temperatures with AMSR2 and SSMIS measurements intercalibrated within the GPM constellation across a wide frequency range from 6.9 GHz and 91.65 GHz. Although the seasonal trends in the simulated and measured brightness temperatures mostly agree with each other, errors and biases may exist between them mostly at frequencies between 10.65 GHz and 37 GHz. Considering the fact that the

Remote Sens. 2022, 14, 2258 17 of 23

simulation results agree well with the measurements at the lowest frequencies—i.e., 6.9 GHz and 7.3 GHz—and the highest—i.e., 89 GHz and 91.65 GHz—which reflect the properties of the deep ice and near surface, we conclude that the sources of these errors are likely related to the spatial and temporal variations in the physical temperature, density, and grain size of the firn layers between ~0.2 m and ~15.1 m (average depths of sensitivity associated with frequencies from 10.65 GHz and 37 GHz) not being accurately represented by the physical models used for these firn properties. Note that these models have been developed mainly based on the local in situ measurements near Concordia Station whereas the satellite footprints cover areas as large as tens of kilometers in radius. High accuracy in simulations at the highest frequencies, on the other hand, eliminates the probability of large biases due to atmospheric conditions.

Using the validated microwave radiation model, a new parameter called the average firn depth of sensitivity, a metric which quantifies the depth where the firn properties significantly influence the surface brightness temperatures, has been introduced as a function of frequency. It has been demonstrated that the average depth of sensitivity decreases with frequency, thus enabling wideband or multi-frequency microwave radiometry to probe the Antarctic firn from the surface to deep isothermal ice. Regarding the AMSR2 and SSMIS measurements, the probing range has been found from the surface to ~40 m depth.

Considering the electrical properties of the firn and the microwave radiation model, it is obvious that firn density and grain size profiles have a significant impact on the surface brightness temperatures; thus, they can be estimated using the radiometer measurements. For instance, firn density fluctuations discussed in Section 2.1.1 determine the reflection and transmission of electromagnetic radiation among firn layers, which in turn influence surface brightness temperatures. Higher density fluctuations result in more internal reflections, thus less surface emission and lower brightness temperatures. This phenomenon may explain the brightness temperature differences between Concordia and Vostok Stations shown in Figures 9 and 10 where the brightness temperatures over Concordia Station are higher than those over Vostok Station, especially at intermediate and high frequencies. Considering that the differences are smaller in vertical polarization, which is less susceptible to internal reflections [41], larger density fluctuations were expected at Vostok Station near the surface. In Section 3.1.3, a simple retrieval study for these profiles has been discussed for Concordia Station. To mimic the measurements over Vostok Station, another retrieval study has been performed. Assuming that physical temperature profiles are similar at Vostok and Concordia Stations, a density profile, described by the $\sigma_{density}$ values versus depth shown in Figure 15—which, as expected, was higher near the surface—has been retrieved. As seen in Figure 16, the retrieved density profile provides a relatively good match between the simulated brightness temperatures and satellite measurements over Vostok Station, except the biases at the intermediate frequencies, reasons for which have been discussed previously. Note that the overall differences between the simulated and measured brightness temperatures are larger for Vostok Station than those for Concordia Station. We suppose that the reason for these larger errors is the lack of in situ data for Vostok Station, as firn properties in this study are modeled mainly based on the Concordia measurements, such as internal firn temperatures, given in Figure 4. Nevertheless, the Vostok results are still important to demonstrate that the brightness temperatures can be modified by varying the firn density profiles to reflect the changes similar to the ones observed between the two stations and such variations in density profiles can be retrieved using satellite measurements.

Physical temperature of the firn is another major factor determining the surface brightness temperature and can be probed at different depths using microwave radiometry. This can be demonstrated by investigating the correlations between the brightness temperatures measured by the GPM radiometers and the physical temperatures of the Antarctic firn at average depths of sensitivity associated with the GPM frequencies. Figure 17 illustrates these correlations at Concordia Station. The correlations have been demonstrated by co-plotting the deviations of the measured brightness and physical temperatures around their annual

Remote Sens. 2022, 14, 2258 18 of 23

mean. As mentioned previously, deep firn is isothermal; thus, no significant variations in brightness temperatures at 6.9 GHz, 7.3 GHz, and 10.65 GHz have been observed. Similarly, physical firn temperatures at 41.4 m, 37 m, and 15.1 m depths, i.e., average depths of sensitivity for 6.9 GHz, 7.3 GHz, and 10.65 GHz, follow a constant pattern throughout the year, showing a high correlation. On the other hand, as frequency increases, i.e., as the average depths of sensitivity decrease, the brightness temperatures at higher frequencies reflect the seasonal physical temperature variations in shallow firn. For example, at 89 GHz and 91.65 GHz, the measured brightness temperatures vary ~35 K between summer and winter. On the other hand, the physical temperatures at the firn surface deviate from the annual mean in a similar manner. These high correlations confirm the potential of extracting thermal properties of polar firn using wideband or multifrequency radiometer such as the GPM radiometer constellation.

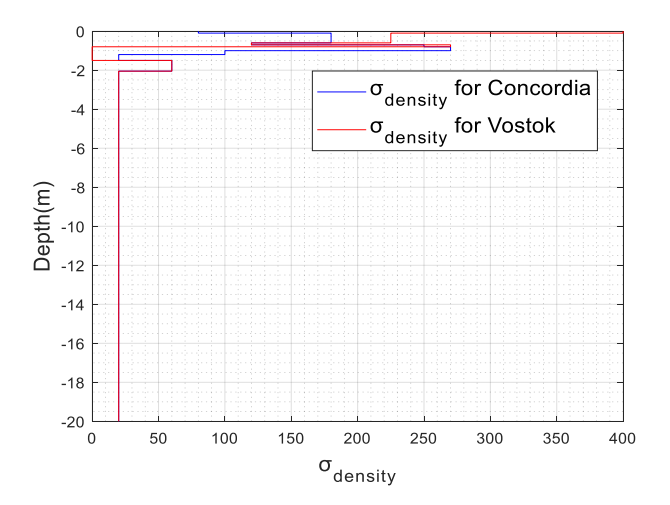


Figure 15. $\sigma_{density}$ profiles at Concordia and Vostok Stations to match calculated and measured brightness temperatures. Note the differences near the surface.

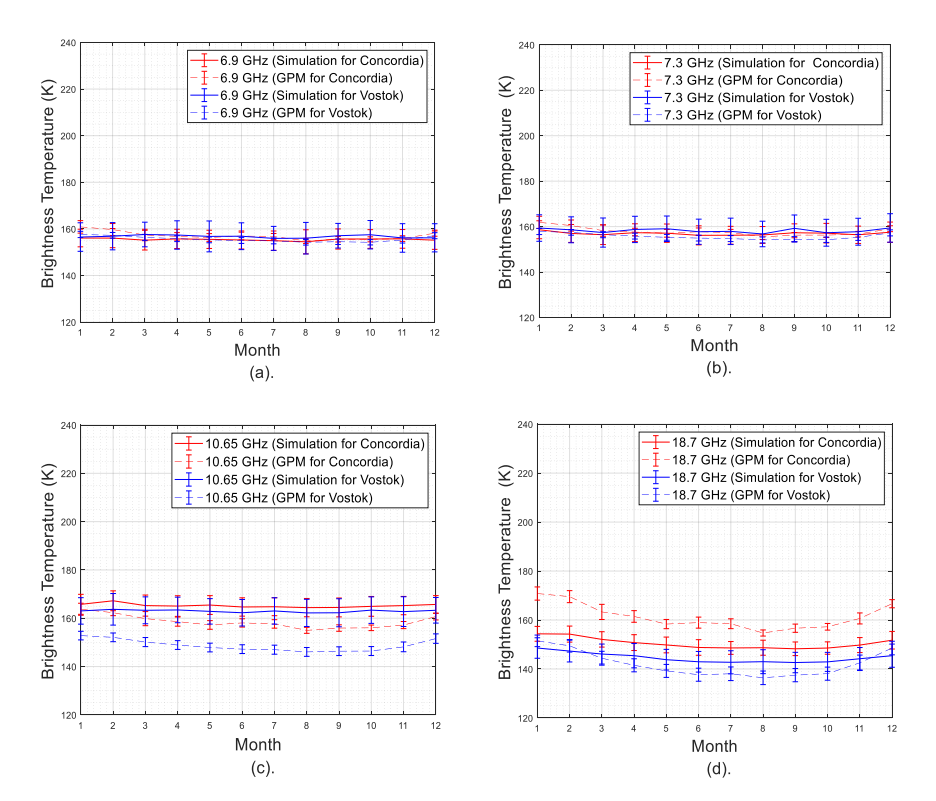


Figure 16. Cont.

Remote Sens. 2022, 14, 2258

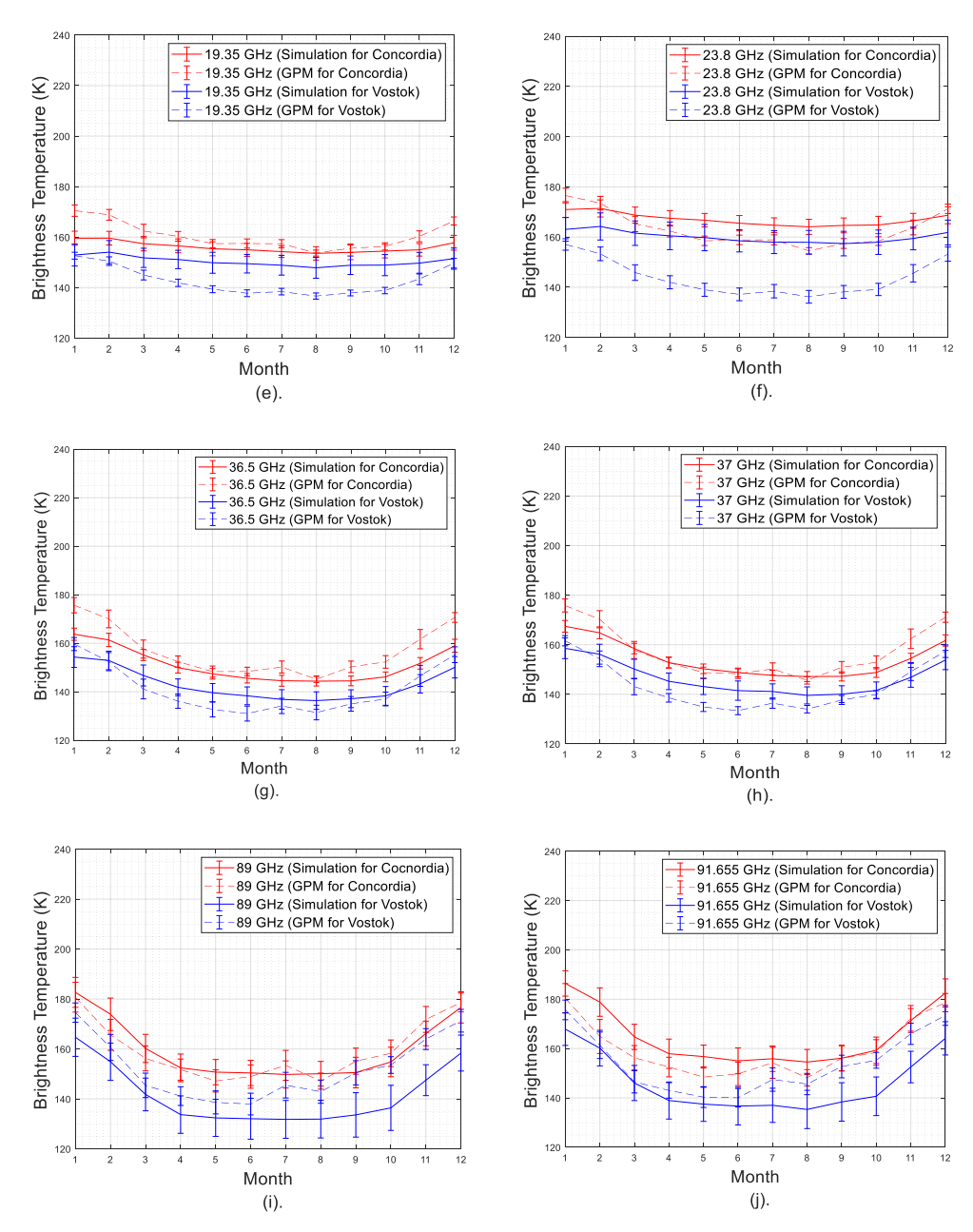


Figure 16. Comparative analysis of calculated and measured brightness temperatures at Concordia and Vostok Stations at frequencies (a) 6.9 GHz, (b) 7.3 GHz, (c) 10.65 GHz, (d) 18.7 GHz, (e) 19.35 GHz, (f) 23.8 GHz, (g) 36.5 GHz, (h) 37 GHz, (i) 89 GHz, and (j) 91.65 GHz.

Remote Sens. 2022, 14, 2258 20 of 23

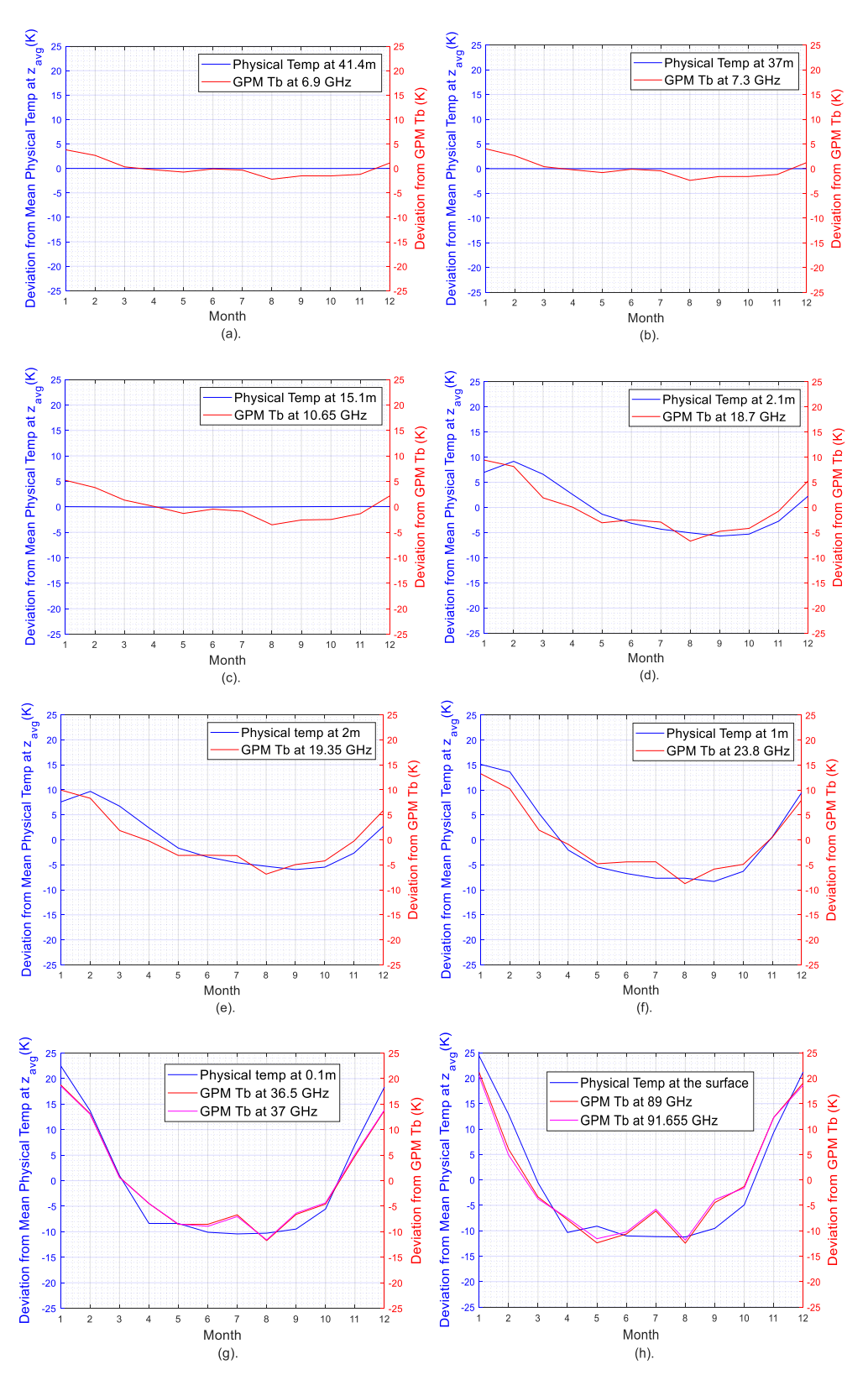


Figure 17. Correlation between GPM-measured brightness temperatures at (a) 6.9 GHz, (b) 7.3 GHz, (c) 10.65 GHz, (d) 18.7 GHz, (e) 19.35 GHz, (f) 23.8 GHz, (g) 36.5–37 GHz, and (h) 89–91.65 GHz and physical firn temperatures at the associated average depths of sensitivity (a) 41.4 m, (b) 37 m, (c) 15.1 m, (d) 2.1 m, € 2 m, (f) 1 m, (g) 0.2 m, and (h) surface. The high correlation between brightness and physical temperatures imply that multifrequency GPM observations can be utilized to profile internal firn temperatures versus depth.

Remote Sens. 2022, 14, 2258 21 of 23

4. Discussion

This study, based on a simple microwave emission model, demonstrates the potential for wideband microwave radiometers such as the GPM constellation to characterize the Antarctic firn in terms of its internal temperature profiles and density properties. It has been demonstrated that the GPM constellation has the potential of profiling the internal physical temperature of the Antarctic firn, which was highlighted by the strong correlation between the GPM brightness temperatures at different frequencies and the physical firn temperatures at the associated depths of sensitivity. In addition, the differences between the brightness temperatures observed over Concordia and Vostok Stations could be simulated by varying the depth-dependent firn density parameters, which suggests that the retrieval of density profiles are also possible.

Note that several studies have been published before regarding the passive microwave remote sensing of the polar firn in which simulated brightness temperatures could be fine-tuned to minimize the bias with satellite measurements [4,16–18]. However, those studies were mostly limited to the 10.65 GHz to 37 GHz frequency range, i.e., intermediate frequencies in this study. This paper, on the other hand, presents the first attempt to utilize a much larger frequency spectrum from 6.9 GHz to 91.65 GHz, i.e., the entire microwave spectrum from C-band to W-band, for a much comprehensive analysis where minimizing biases between simulations and satellite measurements were challenging. However, utilizing all this spectrum, we can characterize the Antarctic firn from the surface to the deep firn by changing the density and grain size profiles as a function of depth with fine vertical resolutions which enables us to retrieve non-uniform variations in firn density and grain with respect to depth as shown in Figure 12. Such retrievals are indeed needed as in situ measurements of firn density and grain size profiles demonstrate similar depth-dependent characteristics [16].

Future studies will include utilizing more comprehensive coherent and incoherent forward electromagnetic models discussed in [19] with additional variables such as internal temperature parameters to further tune and revise the simulated brightness temperatures and incorporating additional radiometer measurements at different frequencies, such as SMAP's 1.4 GHz observations [42]. This will help to validate the initial conclusions presented in this paper, decrease the errors in brightness temperature simulations, and, with proper retrieval algorithms, lead to estimation studies for a more inclusive set of subsurface geophysical parameters over larger and deeper regions within the Antarctic Ice Sheet. Moreover, assimilation of the additional radiometer measurements as well as the lowest AMSR2 frequency channels, 6.9 GHz and 7.3 GHz, into the set of intercalibrated radiometer products should be investigated to achieve better consistency across all frequencies utilized for the characterization of the Antarctic firn through passive remote sensing.

Author Contributions: Conceptualization, M.A. and R.K.; methodology, M.A. and R.K.; software, M.A., R.K., D.K., J.A.D. and P.A.; validation, M.A., R.K.; formal analysis, M.A. and R.K.; investigation, M.A. and R.K.; resources, M.A., R.K., D.K. and P.A.; data curation, M.A., R.K., D.K. and P.A.; writing—original draft preparation, M.A. and R.K.; writing—review and editing, M.A. and R.K.; visualization, M.A. and R.K.; supervision, M.A.; project administration, M.A.; funding acquisition, M.A. All authors have read and agreed to the published version of the manuscript.

Funding: This research was funded by the National Science Foundation, grant number 1844793.

Data Availability Statement: The data presented in this study are openly available in the United States Antarctic Program Data Center (USAP-DC) at https://www.usap-dc.org/view/project/p001 0206 (accessed on 19 March 2022).

Acknowledgments: GPM intercalibrated brightness temperature data are available at NASA Goddard Space Flight Center's Precipitation Processing System (PPS) FTP [39]. 6.9 GHz and 7.3 GHz AMSR2 brightness temperature measurements have been obtained from JAXA through the Globe Portal System (G-Portal) [40].

Conflicts of Interest: The authors declare no conflict of interest.

Remote Sens. **2022**, 14, 2258 22 of 23

References

1. Aksoy, M.; Johnson, J.T.; Jezek, K.C.; Durand, M.; Drinkwater, M.; Macelloni, G.; Tsang, L. An examination of multi-frequency microwave radiometry for probing subsurface ice sheet temperature. In Proceedings of the 2014 IEEE Geoscience and Remote Sensing Symposium (IGARSS), Quebec City, QC, Canada, 13–18 July 2014; pp. 3614–3617. [CrossRef]

- 2. Solomon, S.; Manning, M.; Marquis, M.; Qin, D. Climate Change 2007—The Physical Science Basis: Working Group I Contribution to the Fourth Assessment Report of the IPCC; Cambridge University Press: Cambridge, UK, 2007; Volume 4.
- 3. Picard, G.; Royer, A.; Arnaud, L.; Fily, M. Influence of meter-scale wind-formed features on the variability of the microwave brightness temperature around Dome C in Antarctica. *Cryosphere* **2014**, *8*, 1105–1119. [CrossRef]
- 4. Turner, J.; Colwell, S.R.; Marshall, G.J.; Lachlan-Cope, T.A.; Carleton, A.M.; Jones, P.D.; Lagun, V.; Reid, P.A.; Iagovkina, S. Antarctic climate change during the last 50 years. *Int. J. Climatol.* **2005**, 25, 279–294. [CrossRef]
- 5. Steig, E.J.; Schneider, D.P.; Rutherford, S.D.; Mann, M.E.; Comiso, J.C.; Shindell, D.T. Warming of the Antarctic ice-sheet surface since the 1957 International Geophysical Year. *Nature* **2009**, 457, 459. [CrossRef] [PubMed]
- 6. Jezek, K.C.; Johnson, J.T.; Drinkwater, M.R.; Macelloni, G.; Tsang, L.; Aksoy, M.; Durand, M. Radiometric approach for estimating relative changes in intraglacier average temperature. *IEEE Trans. Geosci. Remote Sens.* **2014**, *53*, 134–143. [CrossRef]
- 7. Johnson, J.T.; Jezek, K.C.; Aksoy, M.; Bringer, A.; Yardim, C.; Andrews, M.; Chen, C.C.; Belgiovane, D.; Leuski, V.; Durand, M.; et al. The Ultra-wideband Software-Defined Radiometer (UWBRAD) for ice sheet internal temperature sensing: Results from recent observations. In Proceedings of the 2016 IEEE Geoscience and Remote Sensing Symposium (IGARSS), Beijing, China, 10–15 July 2016; pp. 7085–7087. [CrossRef]
- 8. Duan, Y.; Durand, M.; Jezek, K.; Yardim, C.; Bringer, A.; Aksoy, M.; Johnson, J. Testing the feasibility of a bayesian retrieval of greenland ice sheet internal temperature from ultra-wideband software-defined microwave radiometer (UWBRAD) measurements. In Proceedings of the 2016 IEEE Geoscience and Remote Sensing Symposium (IGARSS), Beijing, China, 10–15 July 2016; pp. 7092–7093. [CrossRef]
- 9. Yardim, C.; Johnson, J.T.; Jezek, K.C.; Andrews, M.J.; Durand, M.; Duan, Y.; Tan, S.; Tsang, L.; Brogioni, M.; Macelloni, G.; et al. Greenland Ice Sheet Subsurface Temperature Estimation Using Ultrawideband Microwave Radiometry. *IEEE Trans. Geosci. Remote Sens.* 2022, 60, 1–12. [CrossRef]
- Andrews, M.; Johnson, J.T.; Jezek, K.; Li, H.; Bringer, A.; Chen, C.; Belgiovane, D.J.; Leuski, V.; Macelloni, G.; Brogioni, M. The Ultrawideband Software-Defined Microwave Radiometer: Instrument Description and Initial Campaign Results. *IEEE Trans. Geosci. Remote Sens.* 2018, 56, 5923–5935. [CrossRef]
- 11. Fujita, S.; Goto-Azuma, K.; Hirabayashi, M.; Hori, A.; Iizuka, Y.; Motizuki, Y.; Motoyama, H.; Takahashi, K. Densification of layered firn in the ice sheet at Dome Fuji, Antarctica. *J. Glaciol.* **2016**, *62*, 103–123. [CrossRef]
- 12. Herron, M.M.; Langway, C.C. Firn densification: An empirical model. J. Glaciol. 1980, 25, 373–385. [CrossRef]
- 13. Zwally, H.J.; Giovinetto, M.B.; Li, J.; Cornejo, H.G.; Beckley, M.A.; Brenner, A.C.; Saba, J.L.; Yi, D. Mass changes of the Greenland and Antarctic ice sheets and shelves and contributions to sea-level rise: 1992–2002. *J. Glaciol.* 2005, 51, 509–527. [CrossRef]
- 14. Alley, R.B.; Bolzan, J.F.; Whillans, I.M. Polar firn densification and grain growth. Ann. Glaciol. 1982, 3, 7–11. [CrossRef]
- 15. Nye, J.F. Correction factor for accumulation measured by the thickness of the annual layers in an ice sheet. *J. Glaciol.* **1963**, *4*, 785–788. [CrossRef]
- Brucker, L.; Picard, G.; Arnaud, L.; Barnola, J.M.; Schneebeli, M.; Brunjail, H.; Lefebvre, E.; Fily, M. Modeling time series of microwave brightness temperature at Dome C, Antarctica, using vertically resolved snow temperature and microstructure measurements. J. Glaciol. 2011, 57, 171–182. [CrossRef]
- 17. Brucker, L.; Picard, G.; Fily, M. Snow grain-size profiles deduced from microwave snow emissivities in Antarctica. *J. Glaciol.* **2010**, 56, 514–526.
- 18. Picard, G.; Brucker, L.; Fily, M.; Gallée, H.; Krinner, G. Modeling time series of microwave brightness temperature in Antarctica. *J. Glaciol.* **2009**, *55*, 537–551. [CrossRef]
- 19. Tan, S.; Aksoy, M.; Brogioni, M.; Macelloni, G.; Durand, M.; Jezek, K.C.; Wang, T.L.; Tsang, L.; Johnson, J.T.; Drinkwater, M.R.; et al. Physical models of layered polar firn brightness temperatures from 0.5 to 2 GHz. *IEEE J. Sel. Top. Appl. Earth Obs. Remote Sens.* **2015**, *8*, 3681–3691. [CrossRef]
- 20. Jezek, K.C.; Johnson, J.T.; Tan, S.; Tsang, L.; Andrews, M.J.; Brogioni, M.; Macelloni, G.; Durand, M.; Chen, C.C.; Belgiovane, D.J.; et al. 500–2000-MHz brightness temperature spectra of the northwestern greenland ice sheet. *IEEE Trans. Geosci. Remote Sens.* 2017, 56, 1485–1496. [CrossRef]
- 21. Durand, G.; Weiss, J. EPICA Dome C Ice Cores Grain Radius Data. IGBP PAGES/World Data Center for Paleoclimatology Data Contribution Series # 2004-039; NOAA/NGDC Paleoclimatology Program: Boulder, CO, USA, 2004.
- Baker, I.; Obbard, R. Microstructural Location and Composition of Impurities in Polar Ice Cores; US Antarctic Program (USAP) Data Center: Boulder, CO, USA, 2010.
- 23. Matzler, C.; Wegmuller, U. Dielectric properties of freshwater ice at microwave frequencies. *J. Phys. D Appl. Phys.* **1987**, 20, 1623. [CrossRef]
- 24. Mätzler, C. Thermal Microwave Radiation: Applications for Remote Sensing; IET: London, UK, 2006; Volume 52.
- 25. Shih, S.E.; Ding, K.H.; Kong, J.A.; Yang, Y.E. Modeling of millimeter wave backscatter of time-varying snowcover. *Prog. Electromagn. Res.* **1997**, *16*, 305–330. [CrossRef]

Remote Sens. 2022, 14, 2258 23 of 23

26. Tsang, L.; Kong, J.A.; Ding, K.H.; Ao, C.O. *Scattering of Electromagnetic Waves: Numerical Simulations*; John Wiley & Sons: Hoboken, NJ, USA, 2004; Volume 25.

- 27. Proksch, M.; Mätzler, C.; Wiesmann, A.; Lemmetyinen, J.; Schwank, M.; Löwe, H.; Schneebeli, M. MEMLS3a: Microwave Emission Model of Layered Snowpacks adapted to include backscattering. *Geosci. Model Dev.* **2015**, *8*, 2611–2626. [CrossRef]
- 28. Pan, J.; Durand, M.; Sandells, M.; Lemmetyinen, J.; Kim, E.J.; Pulliainen, J.; Kontu, A.; Derksen, C. Differences Between the HUT Snow Emission Model and MEMLS and Their Effects on Brightness Temperature Simulation. *IEEE Trans. Geosci. Remote Sens.* 2016, 54, 2001–2019. [CrossRef]
- 29. Matzler, C. Relation between grain size and correlation length of snow. J. Glaciol. 2002, 48, 461–466. [CrossRef]
- 30. Wiesmann, A.; Christian, M.; Weise, T. Radiometric and structural measurements of snow samples. *Radio Sci.* **1998**, *3*, 273–289. [CrossRef]
- 31. Recommendation ITU-R P.835-6. Attenuation by Atmospheric Gases. Available online: https://www.itu.int/dms_pubrec/itu-r/rec/p/R-REC-P.835-6-201712-I!!PDF-E.pdf (accessed on 15 July 2020).
- 32. Smith, E.A.; Asrar, G.; Furuhama, Y.; Ginati, A.; Mugnai, A.; Nakamura, K.; Adler, R.F.; Chou, M.D.; Desbois, M.; Durning, J.F.; et al. International global precipitation measurement (GPM) program and mission: An overview. In *Measuring Precipitation from Space*; Springer: Dordrecht, The Netherlands, 2007; pp. 611–653.
- 33. Meet the Members of NASA's GPM Constellation. Available online: https://www.nasa.gov/content/goddard/meet-the-members-of-nasas-gpmconstellation (accessed on 14 June 2017).
- 34. NASA. Available online: https://pmm.nasa.gov/GPM (accessed on 18 July 2021).
- 35. Kunkee, D.B.; Poe, G.A.; Boucher, D.J.; Swadley, S.D.; Hong, Y.; Wessel, J.E.; Uliana, E.A. Design and evaluation of the first special sensor microwave imager/sounder. *IEEE Trans. Geosci. Remote Sens.* **2008**, *46*, 863–883. [CrossRef]
- 36. Imaoka, K.; Kachi, M.; Kasahara, M.; Ito, N.; Nakagawa, K.; Oki, T. Instrument performance and calibration of AMSR-E and AMSR2. *Int. Arch. Photogramm. Remote Sens. Spat. Inf. Sci.* **2010**, *38*, 13–18.
- 37. Chang, P.; Jelenak, Z.; Alsweiss, S.; Sapp, J.; Meyers, P.; Ferraro, R. An overview of NOAA's GCOM-W1/AMSR-2 product processing and utilization. In Proceedings of the 2019 IEEE Geoscience and Remote Sensing Symposium (IGARSS), Yokohama, Japan, 28 July–2 August 2019; pp. 8780–8783. [CrossRef]
- 38. Berg, W.; Bilanow, S.; Chen, R.; Datta, S.; Draper, D.; Ebrahimi, H.; Farrar, S.; Jones, W.L.; Kroodsma, R.; McKague, D.; et al. Intercalibration of the GPM microwave radiometer constellation. *J. Atmos. Ocean. Technol.* **2016**, *33*, 2639–2654. [CrossRef]
- 39. Precipitation Processing System. Available online: https://pps.gsfc.nasa.gov/ (accessed on 11 July 2021).
- 40. G-Portal, Globe Portal System. Available online: https://gportal.jaxa.jp/gpr/?lang=en (accessed on 18 July 2021).
- 41. Picard, G.; Brucker, L.; Roy, A.; Dupont, F.; Fily, M.; Royer, A. Simulation of the microwave emission of multi-layered snowpacks using the dense media radiative transfer theory: The DMRT-ML model. *Geosci. Model Dev. Discuss.* **2012**, *5*, 3647–3694. [CrossRef]
- 42. Entekhabi, D.; Eni, G.N.; Peggy, E.N.; Kent, H.K.; Wade, T.C.; Edelstein, W.N.; Entin, J.K.; Goodman, S.D.; Jackson, T.J.; Johnson, J.; et al. The soil moisture active passive (SMAP) mission. *Proc. IEEE* **2010**, *98*, 704–716. [CrossRef]